Editors' Suggestion

Enhanced quality factors at resonance in acoustofluidic cavities embedded in matched elastic metamaterials

Valdemar Frederiksen* and Henrik Bruus†

Department of Physics, Technical University of Denmark, DTU Physics Building 309, DK-2800 Kongens Lyngby, Denmark

(Received 1 November 2025; revised 5 March 2026; accepted 13 March 2026; published 11 May 2026)

We show that by embedding a liquid-filled acoustofluidic cavity in a metamaterial, the quality factor of the cavity at selected acoustic resonance modes can be enhanced by 2–3 orders of magnitude relative to a comparable conventional cavity by matching the coarse-grained elastic moduli of the metamaterial to the acoustic properties of the liquid. The corresponding decrease in dissipation in the cavities is caused by the synchronized motion of the metamaterial and the liquid, which strongly suppresses the resulting acoustic streaming. The weak streaming combined with the enhanced quality factor enables fast acoustophoretic focusing of submicron particles in the cavity.

DOI: 10.1103/vcxl-g1pb

I. INTRODUCTION

The quality factor Q of an acoustic resonance mode in a liquid-filled acoustofluidic cavity embedded in an elastic solid is limited by dissipation in the liquid, mainly due to the large stresses in the thin viscous boundary layers near the elastic walls of the cavity. For megahertz ultrasound resonance modes in typical water-filled acoustofluidic cavities with kinematic viscosity ν at angular frequency ω, Q factors are measured in the range 10–600 [1], a value set by the relevant length scale of the cavity relative to the thickness $\delta = \sqrt{2\nu/\omega}$ of the viscous boundary layer [2]. For the long, straight, box-shaped cavity of length L, width W, and height H, with $H < W \ll L$, studied in Refs. [1,2], it is found that $Q = H/\delta$. Given a typical height $H = 160$ μm and a standing half-wave along the width $W = 375$ μm with a resonance frequency of 2 MHz, we have the boundary-layer width $\delta = 0.4$ μm, and thus $Q = 400$. The same physics, with similar magnitudes $Q \approx R/\delta$, is found theoretically for circular cross sections of radius R [3].

In the above typical example, the boundary layer is formed by viscous friction in the liquid, as the acoustic velocity of the liquid changes from its bulk value v_1 to zero at the nearly rigid wall over a distance δ. The smallness of δ is the reason that the dissipation $\dot{W}_{\mathrm{BL}} \approx \eta(v_1/\delta)^2$ in the boundary layer dominates the total dissipation in the system. The Q factor may be increased considerably simply by removing the boundary layer.

In this paper we show that the boundary layer may be removed, or at least strongly suppressed, by embedding the acoustic cavity not in a conventional elastic solid, denoted by superscript "sl," but instead in an elastic metamaterial denoted by superscript "mm," as illustrated in the conceptual sketch shown in Fig. 1. By tuning the geometrical parameters of the metamaterial such that its coarse-grained elastic moduli essentially equal the corresponding moduli of the liquid, it is possible at a given resonance to match the vibrational velocity $\partial_t \mathbf{u}$ of the metamaterial to the acoustic velocity $\mathbf{v}_1$ of the liquid at the solid-liquid interface of the cavity. This matching suppresses the boundary layer, so that the dissipation of the system is limited by the small bulk dissipation of the liquid, and the Q factor increases to approximately 10^5.

The paper is organized as follows. In Sec. II we present the theory of acoustic cavities embedded in an elastic metamaterial. In Sec. III we introduce a specific two-dimensional (2D) model, which is simulated numerically in Sec. IV using the finite-element software COMSOL Multiphysics, as well as solved analytically for a simplified case in Sec. III C. The 2D model is subsequently extended to a 3D model, briefly studied in Sec. V. Finally, in Secs. VI and VII we discuss the results and present our conclusions and outlook regarding the focusing of submicron particles. Animations of selected results, together with some COMSOL scripts, are provided in the Supplemental Material [4].

II. THEORY

A. The model system

In the main part of this work, our proposed system is assumed to be translationally invariant in the length direction x. From the infinitely many designs implied in Fig. 1, we have chosen to work with the specific type of structure

*Contact author: valde.freder@gmail.com
†Contact author: bruus@fysik.dtu.dk

 © 2026 American Physical Society

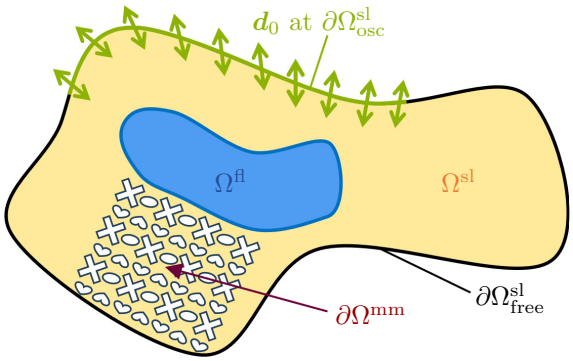

FIG. 1. A conceptual sketch of the cross section of the long, straight model system with three types of domains: a fluid cavity or channel Ω^{fl} (blue) embedded in an elastic solid Ω^{sl} (beige) that contains a metamaterial subdomain Ω^{mm} (beige with white structures). The outer surface of the solid is divided into the free part $\partial\Omega^{\mathrm{sl}}_{\mathrm{free}}$ (black) and the oscillating, actuated part $\partial\Omega^{\mathrm{sl}}_{\mathrm{osc}}$ (green), where the green double arrows represent the oscillation amplitude vector $\mathbf{d}_0$.

having the rectangular 2D cross section sketched in Fig. 2. This particular design allows us to find the approximate analytical solution discussed in Sec. III C below using a coarse-grained version of the metamaterial, which not only elucidates the physical cause of the liquid-wall synchronization but also provides initial values of the geometrical parameters of the actual metamaterial to be optimized. Its simplicity furthermore allows a straightforward extension to the 3D model, briefly studied in Sec. V below, obtained by extruding the 2D cross section along the axial direction, resulting in a straight device of length L.

In the 2D cross section, a fluid-filled cavity Ω^{fl} circumscribing a rectangle of width W^{fl} and height H^{fl} is surrounded by a solid material region Ω^{sl}, which is subdivided into four domains. The base $\Omega^{\mathrm{sl}}_{\mathrm{base}}$ is a large rectangular block of regular solid material of width W^{sl} and height H^{sl}, with a free surface to the left. The lid $\Omega^{\mathrm{sl}}_{\mathrm{lid}}$ is a thin rectangular region of regular solid material of width $W^{\mathrm{sl}}_{\mathrm{lid}}$ with a prescribed time-harmonic displacement $\mathbf{u}^{\mathrm{phys}} = d_0\cos(\omega t)\,\mathbf{e}_y$ on its rightmost boundary. The remaining two rectangular regions $\Omega^{\mathrm{mm}}_{\mathrm{up}}$ and $\Omega^{\mathrm{mm}}_{\mathrm{down}}$ above and below the cavity consist of a mechanically periodic metamaterial, with a unit cell $\Omega^{\mathrm{mm}}_{\mathrm{cell}}$ of height H_{cell} and width W_{cell}, shown in the inset of Fig. 2, repeated $N_y \times N_z$ times along y and z, respectively. The small-scale geometry of $\Omega^{\mathrm{mm}}_{\mathrm{cell}}$ is optimized to make the metamaterial move in sync with the fluid in the cavity. We treat all acoustic fields g_1 to be complex-valued with a harmonic time dependence $\mathrm{e}^{-\mathrm{i}\omega t}$, such that the real part corresponds to the true physical field g^{phys},

$$g^{\mathrm{phys}}(\mathbf{r},t) = \mathrm{Re}[g_1(\mathbf{r})\,\mathrm{e}^{-\mathrm{i}\omega t}]. \tag{1}$$

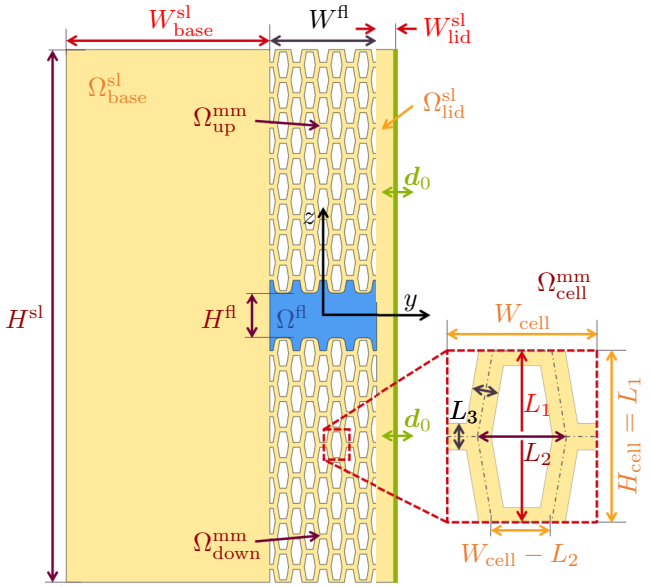

FIG. 2. The 2D model device consisting of five domains: the solid base $\Omega^{\mathrm{sl}}_{\mathrm{base}}$, the fluid channel Ω^{fl}, the solid lid $\Omega^{\mathrm{sl}}_{\mathrm{lid}}$, and the two metamaterial walls $\Omega^{\mathrm{mm}}_{\mathrm{up}}$ and $\Omega^{\mathrm{mm}}_{\mathrm{down}}$, each being an $(N_y \times N_z)$ metamaterial, here $(N_y \times N_z) = (4 \times 8)$, with the elongated hexagonal unit cell $\Omega^{\mathrm{mm}}_{\mathrm{cell}}$ of height H_{cell} and width W_{cell} shown enlarged in the inset. The device is actuated on the outer rightmost surface (green line) with a time-harmonic uniform displacement amplitude of d_0 (green arrows), while all other walls are free to move, having zero-stress conditions.

B. The fluid domain

To model the acoustic behavior of the coupled fluid-solid system, we follow our previous work [2,5] and first consider the governing equations in the fluid domain Ω^{fl} in terms of the pressure p, velocity $\mathbf{v}$, and density ρ^{fl}, namely the continuity and Navier–Stokes equations,

$$\partial_t \rho^{\mathrm{fl}} = -\nabla\cdot(\rho^{\mathrm{fl}}\mathbf{v}), \tag{2a}$$

$$\rho^{\mathrm{fl}}\partial_t\mathbf{v} = \nabla\cdot\boldsymbol{\sigma}^{\mathrm{fl}} - (\rho^{\mathrm{fl}}\mathbf{v}\cdot\nabla)\mathbf{v}, \tag{2b}$$

where the fluid stress tensor $\boldsymbol{\sigma}^{\mathrm{fl}}$ is given in terms of p, $\mathbf{v}$, and the respective shear and bulk viscosity η and η^b,

$$\boldsymbol{\sigma}^{\mathrm{fl}} = \big[-p + \big(\eta^b - \tfrac{2}{3}\eta\big)\nabla\cdot\mathbf{v}\big]\mathbf{I} + \eta[\nabla\mathbf{v} + (\nabla\mathbf{v})^{\mathsf{T}}]. \tag{3}$$

At the fluid-solid interface, which is the boundary $\partial\Omega^{\mathrm{fl}}$ of the fluid domain Ω^{fl} with normal vector $\mathbf{n}$, the boundary conditions are continuity in velocity and surface stress,

$$\mathbf{v} = \partial_t\mathbf{u} \quad \text{at } \partial\Omega^{\mathrm{fl}}, \tag{4a}$$

$$\boldsymbol{\sigma}^{\mathrm{fl}}\cdot\mathbf{n} = \boldsymbol{\sigma}^{\mathrm{sl}}\cdot\mathbf{n} \quad \text{at } \partial\Omega^{\mathrm{fl}}, \tag{4b}$$

where $\boldsymbol{\sigma}^{\mathrm{sl}}$ and $\partial_t\mathbf{u}$ are the stress and velocity of the material surrounding the fluid domain. We solve the above

equations by applying perturbation theory in terms of the acoustic Mach number, assuming fields to become progressively weaker with increasing orders. For the zeroth-order solution, we assume the fluid to be at rest, $\mathbf{v}_0 = \mathbf{0}$, with constant pressure p_0 and density ρ_0^{fl}.

We then assume the first-order fields to be time harmonic, $g_1 = g_1(\mathbf{r})\,\mathrm{e}^{-\mathrm{i}\omega t}$, and relate the first-order pressure and density, $p_1(\mathbf{r}) = \rho_1^{\mathrm{fl}}(c_0^{\mathrm{fl}})^2$, by assuming a constant compressibility $\kappa_0^{\mathrm{fl}} = [\rho_0^{\mathrm{fl}}(c_0^{\mathrm{fl}})^2]^{-1}$, where c_0^{fl} is the sound speed of the wave with wave number $k_0^{\mathrm{fl}} = \omega/c_0^{\mathrm{fl}}$. Finally, we truncate the perturbation expansion and keep only zeroth-, first-, and time-averaged second-order fields,

$$\rho^{\mathrm{fl}}(\mathbf{r},t) = \rho_0^{\mathrm{fl}} + \rho_0^{\mathrm{fl}}\kappa_0^{\mathrm{fl}} p_1(\mathbf{r})\,\mathrm{e}^{-\mathrm{i}\omega t} + \rho_2^{\mathrm{fl}}(\mathbf{r}), \tag{5a}$$

$$p(\mathbf{r},t) = p_0 + p_1(\mathbf{r})\,\mathrm{e}^{-\mathrm{i}\omega t} + p_2(\mathbf{r}), \tag{5b}$$

$$\mathbf{v}(\mathbf{r},t) = \mathbf{v}_1(\mathbf{r})\,\mathrm{e}^{-\mathrm{i}\omega t} + \mathbf{v}_2(\mathbf{r}). \tag{5c}$$

Inserting this expansion into Eq. (2), we obtain the first-order governing equations

$$i\omega\kappa_0^{\mathrm{fl}} p_1 = \nabla\cdot\mathbf{v}_1, \tag{6a}$$

$$i\omega\rho_0^{\mathrm{fl}}\mathbf{v}_1 = \nabla p_1 - \eta\nabla^2\mathbf{v}_1 - \left(\eta^{\mathrm{b}} - \tfrac{2}{3}\eta\right)\nabla(\nabla\cdot\mathbf{v}_1), \tag{6b}$$

which we solve numerically and with which we work analytically moving forward.

Numerically, we also solve for the second-order fields in Ω^{fl}, which are governed by the equations [2,5]

$$\rho_0^{\mathrm{fl}}\nabla\cdot\mathbf{v}_2 + \nabla\cdot\left\langle\rho_1^{\mathrm{fl}}\mathbf{v}_1\right\rangle = 0 \quad \text{in } \Omega^{\mathrm{fl}}, \tag{7a}$$

$$\nabla\cdot\boldsymbol{\sigma}_2^{\mathrm{fl}} - \rho_0^{\mathrm{fl}}\nabla\cdot\langle\mathbf{v}_1\mathbf{v}_1\rangle = \mathbf{0} \quad \text{in } \Omega^{\mathrm{fl}}, \tag{7b}$$

$$\mathbf{v}_2 + \langle(\mathbf{u}_1\cdot\nabla)\mathbf{v}_1\rangle = \mathbf{0} \quad \text{at } \partial\Omega^{\mathrm{fl}}, \tag{7c}$$

where the bracket $\langle A_1 B_1\rangle$ represents the time average over one oscillation period of the product of any two complex-valued first-order fields A_1 and B_1,

$$\langle A_1 B_1\rangle = \tfrac{1}{2}\,\mathrm{Re}[A_1 B_1^*], \tag{8}$$

with the asterisk denoting the complex conjugate.

To characterize the utility of acoustic modes with regard to focusing microparticles by acoustophoresis, we calculate for each mode three useful quantities: the time-averaged acoustic energy density $E_{\mathrm{ac}}^{\mathrm{fl}}$ in the fluid,

$$E_{\mathrm{ac}}^{\mathrm{fl}} = \frac{\kappa_0^{\mathrm{fl}}}{2}\langle p_1 p_1\rangle + \frac{\rho_0^{\mathrm{fl}}}{2}\left\langle v_{1,i}v_{1,i}\right\rangle = \frac{\kappa_0^{\mathrm{fl}}}{4}|p_1|^2 + \frac{\rho_0^{\mathrm{fl}}}{4}|\mathbf{v}_1|^2, \tag{9a}$$

the Rayleigh streaming speed v_2^{Rayl} defined by

$$v_2^{\mathrm{Rayl}} = \frac{3E_{\mathrm{ac}}^{\mathrm{fl}}}{2\rho_0^{\mathrm{fl}}c_0^{\mathrm{fl}}}, \tag{9b}$$

and the spatial average $\langle\!\langle v_2\rangle\!\rangle$ of the magnitude of the streaming velocity $\mathbf{v}_2$,

$$\langle\!\langle v_2\rangle\!\rangle = \frac{1}{\mathcal{V}^{\mathrm{fl}}}\int_{\Omega^{\mathrm{fl}}}|\mathbf{v}_2|\,\mathrm{d}V. \tag{9c}$$

If we imagine placing a spherical particle with radius a inside an acoustic cavity, the particle is subject to an acoustic radiation force $F_{\mathrm{rad}} \sim a^3 k_0^{\mathrm{fl}} E_{\mathrm{ac}}^{\mathrm{fl}}$ pushing it toward the nearest pressure node (or antinode) [6–8]. Simultaneously, a drag force $F_{\mathrm{drag}} \sim 6\pi a\eta v_2$ associated with the acoustic streaming field $\mathbf{v}_2$ will instead tend to pull this particle around in a vortex motion. Consequently, there exists a critical radius $a_c \sim \delta\sqrt{v_2/v_2^{\mathrm{Rayl}}}$, for which $F_{\mathrm{drag}} \sim F_{\mathrm{rad}}$, and below which particle focusing ceases. For polystyrene particles in the box-shaped 2-MHz cavity described in the Introduction, this radius is roughly $a_c \sim 1$ μm [9,10]. For strong focusing of small particles, one therefore needs $E_{\mathrm{ac}}^{\mathrm{fl}}$ to be as high as possible while keeping the streaming field $\mathbf{v}_2$ as low as possible.

C. The solid domains

In the solid domains, we apply linear elastodynamics to solve for the displacement field $\mathbf{u}(\mathbf{r},t)$, such that the Hookean stress tensor $\boldsymbol{\sigma}^{\mathrm{sl}}$ is linear in the strain tensor $\mathbf{s} = \frac{1}{2}[\nabla\mathbf{u} + (\nabla\mathbf{u})^{\mathrm{T}}]$ in terms of the stiffness tensor $\mathbf{C}$,

$$(\boldsymbol{\sigma}^{\mathrm{sl}})_{ij} = (\mathbf{C}:\mathbf{s})_{ij} = C_{ijkl}s_{kl}. \tag{10}$$

The second equality employs index notation, where summation over repeated indices is implied. For isotropic materials, $\mathbf{C}$ can be written in terms of the Voigt coefficients C_{11} and C_{44} as

$$C_{ijkl} = (C_{11} - 2C_{44})\delta_{ij}\delta_{kl} + C_{44}(\delta_{ik}\delta_{jl} + \delta_{il}\delta_{jk}). \tag{11}$$

Consequently, the governing equation for the time-harmonic displacement field $\mathbf{u}$ of the elastic solid is the Cauchy momentum equation [2,5]

$$\mathbf{u}(\mathbf{r},t) = \mathbf{u}_1(\mathbf{r})\,\mathrm{e}^{-\mathrm{i}\omega t}, \tag{12a}$$

$$-\omega^2\rho^{\mathrm{sl}}\mathbf{u}_1 = \nabla\cdot\boldsymbol{\sigma}^{\mathrm{sl}} \quad \text{in } \Omega^{\mathrm{sl}}. \tag{12b}$$

On the boundary of the solid domain, three types of boundary conditions apply: (1) continuity of velocity on the fluid-solid boundaries $\partial\Omega^{\mathrm{fl}}$, which supplements the continuity of stress in Eq. (4b); (2) a prescribed time-harmonic displacement with amplitude d_0 on the actuated part $\partial\Omega_{\mathrm{osc}}^{\mathrm{sl}}$ of the outer boundary; and (3) zero stress on the

remaining free part $\partial\Omega^{\mathrm{sl}}_{\mathrm{free}}$ of the outer boundaries,

$$\mathbf{u}_1 = \frac{\mathrm{i}}{\omega}\mathbf{v}_1 \quad \text{at } \partial\Omega^{\mathrm{fl}}, \tag{13a}$$

$$\mathbf{u}_1 = d_0\,\mathbf{n} \quad \text{at } \partial\Omega^{\mathrm{sl}}_{\mathrm{osc}}, \tag{13b}$$

$$\boldsymbol{\sigma}^{\mathrm{sl}}\cdot\mathbf{n} = \mathbf{0} \quad \text{at } \partial\Omega^{\mathrm{sl}}_{\mathrm{free}}. \tag{13c}$$

We end this section by defining the time-averaged acoustic energy density $E^{\mathrm{sl}}_{\mathrm{ac}}$ within the solid as

$$E^{\mathrm{sl}}_{\mathrm{ac}} = \tfrac{1}{2}\left\langle (C_{ijkl}s_{1,ij})s_{1,kl}\right\rangle + \tfrac{1}{2}\rho^{\mathrm{sl}}\omega^2\left\langle u_{1,i}u_{1,i}\right\rangle. \tag{14}$$

The total time-averaged acoustic energy $\bar{U}_{\mathrm{ac}}$ of the device, the time-averaged acoustic power $\bar{P}_{\mathrm{in}}$ supplied to the device, and the quality factor Q_n of the nth resonance modes at frequency ω_n of the device are thus

$$\bar{U}_{\mathrm{ac}} = \int_{\Omega^{\mathrm{fl}}} E^{\mathrm{fl}}_{\mathrm{ac}}\,\mathrm{d}V + \int_{\Omega^{\mathrm{sl}}} E^{\mathrm{sl}}_{\mathrm{ac}}\,\mathrm{d}V, \tag{15a}$$

$$\bar{P}_{\mathrm{in}} = \int_{\partial\Omega^{\mathrm{sl}}} \left\langle(-\mathrm{i}\omega_n\mathbf{u}_1)\cdot(\boldsymbol{\sigma}^{\mathrm{sl}}_1\cdot\mathbf{n})\right\rangle \mathrm{d}A, \tag{15b}$$

$$Q_n = \frac{\omega_n\bar{U}_{\mathrm{ac}}}{\bar{P}_{\mathrm{in}}}. \tag{15c}$$

D. The metamaterial domains

The metamaterial domains consist of $N_y \times N_z$-arrays of the elongated hexagonal unit cell as specified in Fig. 2 and Table I, which for short is called an $(N_y \times N_z)$ metamaterial. The metamaterial domains are governed by the Cauchy equation with the same material parameters as for the regular solid domains, but of course implemented with the full intricate metamaterial geometry. Once the $N_y \times N_z$ array is constructed, the implementation in COMSOL Multiphysics of the metamaterial is straightforward, and this implementation is used to produce all the results presented in Secs. IV and V below.

However, when making the analytical approximations in Sec. III C below to find a good starting point for the metamaterial optimization, we describe the metamaterial as a homogeneous, anisotropic elastic solid governed by the Cauchy equation with coarse-grained values (superscript "mm") of the displacement field and the material parameters: $\mathbf{u} \to \mathbf{u}^{\mathrm{mm}}$, $\rho^{\mathrm{sl}} \to \rho^{\mathrm{mm}}$, and $C_{ijkl} \to C^{\mathrm{mm}}_{ijkl}$. Most of these coarse-grained quantities are assumed to be local spatial averages of their regular counterparts, e.g., $\rho^{\mathrm{mm}} = (1/W_{\mathrm{cell}}H_{\mathrm{cell}})\int_{\Omega^{\mathrm{mm}}_{\mathrm{cell}}}\rho^{\mathrm{sl}}\,\mathrm{d}V$. The single exception to this rule is C^{mm}_{ijkl}, which instead is defined to satisfy the coarse-grained version of Eq. (10) as follows. On a single unit cell (see the inset of Fig. 2) we apply a constant strain $s_{yy} = d_0/W_{\mathrm{cell}}$ by prescribing a displacement of $\mathbf{u} = d_0\mathbf{e}_y$ on the rightmost edge $\mathcal{E}_R$, a zero displacement $\mathbf{u} = \mathbf{0}$ on the leftmost edge $\mathcal{E}_L$, and the symmetry condition $u_z = 0$ on the top and bottom edges $\mathcal{E}_T$ and $\mathcal{E}_B$. Then the metamaterial values of the elastic coefficients are given by the following averages over the unit cell: $C^{\mathrm{mm}}_{iiyy} = (1/d_0H_{\mathrm{cell}})\int_{\Omega^{\mathrm{mm}}_{\mathrm{cell}}}\sigma_{ii}\,\mathrm{d}A$ for $ii = yy$ and zz. Likewise, by applying a strain $s_{zz} = d_0/H_{\mathrm{cell}}$ on $\mathcal{E}_T$ and zero strain on $\mathcal{E}_B$, we obtain $C^{\mathrm{mm}}_{iizz} = (1/d_0W_{\mathrm{cell}})\int_{\Omega^{\mathrm{mm}}_{\mathrm{cell}}}\sigma_{ii}\,\mathrm{d}A$.

TABLE I. Parameter values used in the model systems. For fused silica, the following parameters are computed from the values listed in Ref. [11]: $\alpha = 6.25\times10^{-5}$ dB/cm $\times$ 0.115 Np/dB $\times$ 100 cm/m, $\gamma = \alpha c_{\mathrm{lo}}/\omega$, $\mathrm{Re}[C_{11}] = \rho c^2_{\mathrm{lo}}$, $\mathrm{Re}[C_{44}] = \rho c^2_{\mathrm{tr}}$, and $\mathrm{Im}[C_{ii}] = -2\gamma\,\mathrm{Re}[C_{ii}]$.

Parameter	Symbol	Value	Unit
Fused silica [11]			
Mass density	ρ^{sl}	2200	kg m^{-3}
Sound speed, longitudinal	c_{lo}	5700	m/s
Sound speed, transverse	c_{tr}	3750	m/s
Attenuation constant at 2 MHz	α	714	μNp/m
Damping coefficient at 2 MHz	γ	0.324	ppm
Elastic modulus 11, real part	$\mathrm{Re}[C_{11}]$	71.5	GPa
Elastic modulus 44, real part	$\mathrm{Re}[C_{44}]$	30.9	GPa
Elastic modulus 11, imag. part	$\mathrm{Im}[C_{11}]$	−46.3	kPa
Elastic modulus 44, imag. part	$\mathrm{Im}[C_{44}]$	−20.0	kPa
Water [12]			
Mass density	ρ^{fl}_0	997.05	kg m^{-3}
Speed of sound	c^{fl}_0	1496.7	m s^{-1}
Dynamic viscosity	η	0.890	mPa s
Bulk viscosity	η^b	2.485	mPa s
Compressibility	κ^{fl}_0	447.7	TPa^{-1}
Geometry, Fig. 2			
Channel height	H^{fl}	160	μm
Channel width	W^{fl}	375	μm
Solid base width	$W^{\mathrm{sl}}_{\mathrm{base}}$	714	μm
Solid lid width	$W^{\mathrm{sl}}_{\mathrm{lid}}$	71	μm
Displacement amplitude	d_0	0.1	nm

III. MODELING THE 2D SYSTEM

A. Materials and geometry of the model

The model to be simulated numerically is defined as follows. The solid material is chosen to be fused silica glass due to its small attenuation constant, and the fluid is water. All parameter values are listed in Table I. The detailed cross-sectional geometry in the y-z plane is shown in Fig. 2, and the model is assumed to be translationally invariant in the out-of-plane x direction. The elongated hexagonal unit cell shown in Fig. 2 is inspired by Ref. [13]. Its initial configuration is chosen to satisfy the requirements for the coarse-grained stiffness and density derived in Sec. III C, and it is computed as described in Sec. IV A.

The design goal of the geometry is to support the first acoustic mode $n = 1$, a standing half-wave resonance inside the rectangular fluid channel of width W^{fl} and height H^{fl}, with a pressure node along the center line at $y = 0$, and

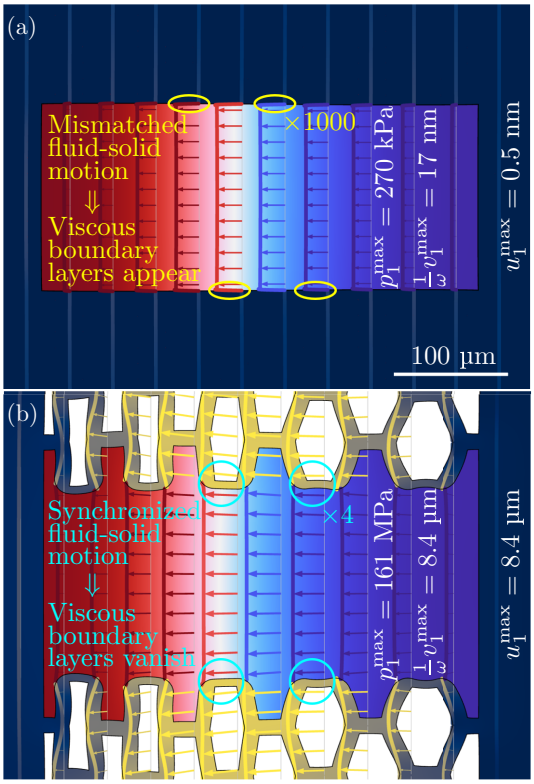

FIG. 3. Simulation results in and near the fluid cavity for $d_0 = 0.1$ nm: color plots of the pressure field p_1 from $-p_1^{max}$ (blue) to p_1^{max} (red) in the fluid and of the magnitude u_1 from zero (dark blue) to u_1^{max} (yellow) of the displacement field $\mathbf{u}_1$ in the solid. The first-order displacements $\mathbf{u}_1$ and $i\omega^{-1}\mathbf{v}_1$ of the solid and fluid are represented by deformed colored lines and colored arrows relative to evenly spaced gray zero-deformation lines. (a) The conventional rectangular cavity with $u_1^{max} = 17$ nm (×1000 for clarity) and $p_1^{max} = 270$ kPa. (b) The optimized cavity using the (5 × 10) metamaterial with the hexagonal unit cell defined in Fig. 2, and with $u_1^{max} = 8.4$ µm (×4 for clarity) and $p_1^{max} = 161$ MPa. Animated versions of the panels and associated COMSOL scripts are given in the Supplemental Material [4].

subsequently to fine-tune this mode to maximize its Q factor Q_1. The obtained systems are then compared against a conventional reference system, in which the metamaterial domains are replaced by solid fused silica.

B. Implementation in COMSOL

The governing equations and boundary conditions of Sec. II are, as in our previous work [2,5,7–9], implemented in the "`Weak Form PDE Interface`" of the commercial finite-element software COMSOL Multiphysics [14]. Examples of numerical solutions are shown in Fig. 3 for both a conventional rectangular fluid-filled channel embedded in an ordinary elastic solid and for an $(N_y \times N_z)$ metamaterial model.

C. An approximate analytical solution

As stated earlier, the goal of this study is to create an acoustofluidic mode without viscous boundary layers, so $\mathbf{v}_1$ must be irrotational [2]. In this case, the first-order governing equations reduce to a Helmholtz equation for p_1, while the velocity field $\mathbf{v}_1$ is proportional to ∇p_1:

$$\nabla^2 p_1 = -(1 + i\gamma^{fl})\frac{\omega^2}{(c_0^{fl})^2} p_1, \tag{16a}$$

$$\mathbf{v}_1 = \frac{-i}{\omega\rho_0^{fl}}\nabla p_1. \tag{16b}$$

Here $\gamma^{fl} = \omega\kappa_0^{fl}(\eta^b + \frac{4}{3}\eta)$ is the dimensionless bulk damping coefficient of the fluid, which for MHz frequencies in water is of order 10^{-5}. A mode is thus matched, or synchronized, with the wall motion if this curl-free bulk velocity along the entire boundary of the fluid domain satisfies the no-slip condition (4a), which in terms of p_1 is

$$\frac{1}{\omega^2\rho_0^{fl}}\nabla p_1 = \mathbf{u}_1 \quad \text{at } \partial\Omega^{fl}. \tag{17}$$

This condition gives us a strong hint about how to construct a cavity with a wall-synchronized resonance mode. We start by assuming that the cavity contains an ideal standing pressure half-wave along the y direction,

$$p_1 = p_1^0 \sin(k_0^{fl} y) \quad \text{with } k_0^{fl} = \frac{\pi}{W^{fl}}. \tag{18}$$

Neglecting γ^{fl}, this mode obeys Eq. (16a) for $\omega = c_0^{fl}k_0^{fl}$. Next, to satisfy the wall-synchronization condition (17), we approximate the actual $(N_y \times N_z)$ metamaterial by its coarse-grained counterpart. The displacement $\mathbf{u}_1^{mm}$ in the two coarse-grained metamaterial regions Ω_{up}^{mm} and Ω_{down}^{mm} may therefore be chosen to be

$$\mathbf{u}_1^{mm} = \frac{p_1^0 k_0^{fl}}{\omega^2\rho_0^{fl}} \cos(k_0^{fl} y)\, \mathbf{e}_y \quad \text{in } \Omega_{up}^{mm} \text{ and } \Omega_{down}^{mm}. \tag{19}$$

Finally, one way to ensure that the displacement field $\mathbf{u}_1$ in the isotropic base solid Ω^{sl} has a vanishing amplitude along the base-metamaterial interface at $y = -\frac{1}{2}W^{fl}$, while maintaining a nonvanishing normal stress, is to choose $\mathbf{u}_1$ to be a quarter of a standing longitudinal displacement wave with a node at $y = -\frac{1}{2}W^{fl}$,

$$\mathbf{u}_1 = u_1^0 \sin\left[k^{sl}\left(y + \tfrac{1}{2}W^{fl}\right)\right]\mathbf{e}_y \quad \text{in } \Omega_{base}^{sl}. \tag{20}$$

From the Cauchy equation (12b) and the continuous-stress boundary conditions in Eq. (4b), this assumption

results in the amplitude and wave-number relations,

$$u_1^0 = \frac{p_1^0}{k^{\mathrm{sl}} C_{11}}, \tag{21a}$$

$$k^{\mathrm{sl}} = k^{\mathrm{fl}} c_0^{\mathrm{fl}} \sqrt{\frac{\rho^{\mathrm{sl}}}{C_{11}}} = k^{\mathrm{fl}} \frac{c_0^{\mathrm{fl}}}{c_0^{\mathrm{sl},L}}, \tag{21b}$$

the quarter-wave width condition,

$$W_{\mathrm{base}}^{\mathrm{sl}} = \frac{\pi}{2k^{\mathrm{sl}}} = \frac{c_0^{\mathrm{sl},L}}{2c_0^{\mathrm{fl}}} W^{\mathrm{fl}}, \tag{22}$$

and the following set of conditions on the coarse-grained metamaterial parameters ρ^{mm} and C_{ijkl}^{mm}:

$$\rho^{\mathrm{mm}} = \rho_0^{\mathrm{fl}}, \qquad C_{iyyy}^{\mathrm{mm}} = \frac{1}{\kappa_0^{\mathrm{fl}}}\delta_{iy}, \qquad C_{izyy}^{\mathrm{mm}} = \frac{1}{\kappa_0^{\mathrm{fl}}}\delta_{iz}. \tag{23}$$

In the limit where the lid thickness $W_{\mathrm{lid}}^{\mathrm{sl}}$ tends to zero and the device height H^{sl} tends to infinity, this system has an almost perfectly matched, or synchronized, resonance mode at $f = c_0^{\mathrm{fl}}/(2W^{\mathrm{fl}}) = 1.996$ MHz. In the following section we show that even in the case of a geometry with finite values of $W_{\mathrm{lid}}^{\mathrm{sl}}$ and H^{sl}, the above coarse-grained values serve as an excellent starting point for the numerical determination of the geometry of actual $(N_y \times N_z)$ metamaterials that support well-synchronized modes.

IV. 2D MODEL: NUMERICAL SIMULATIONS

We now present the main result of our study of the 2D model: the optimization of the $(N_y \times N_z)$ metamaterial to maximize the Q value of the acoustic cavity.

A. Optimizing the system to maximize the Q value

To optimize the metamaterial, we first find an initial metamaterial that satisfies the three criteria listed in Eq. (23). For this, we opt for a hexagonal metamaterial, which has shown high tunability in previous work [13], and which, due to its twofold mirror symmetry, already satisfies the criteria $C_{iyyy}^{\mathrm{mm}} = C_{yyyy}^{\mathrm{mm}}\delta_{iy}$ and $C_{izyy}^{\mathrm{mm}} = C_{zzyy}^{\mathrm{mm}}\delta_{iz}$. By simulation in COMSOL Multiphysics of one unit cell $\Omega_{\mathrm{cell}}^{\mathrm{mm}}$, we calculate the coarse-grained stiffness tensor $\mathbf{C}^{\mathrm{mm}}(L_1, L_2, L_3)$ and adjust the parameters L_1, L_2, and L_3 defined in Fig. 2 until Eq. (23) is satisfied. This results in the values L_1^0, L_2^0, and L_3^0:

$$L_1^0 = \frac{412\,\mu\mathrm{m}}{N_y} \qquad L_2^0 = \frac{206.6\,\mu\mathrm{m}}{N_y} \qquad L_3^0 = \frac{67.9\,\mu\mathrm{m}}{N_y}. \tag{24}$$

Next, using L_1^0, L_2^0, and L_3^0 as initial values for a given choice of (N_y, N_z), we simulate the full system repeatedly using the built-in COMSOL "Optimization Interface" with the unit-cell height L_1 and hole width L_2 as optimization parameters to be changed after each numerical iteration, while keeping the strut width fixed, $L_3 = L_3^0$, until the Q factor of the resonance mode is maximized. The resulting optimized values L_1^{opt} and L_2^{opt} of L_1 and L_2 are listed in Table II. Note that the device height at all times must satisfy $H^{\mathrm{sl}} = H^{\mathrm{fl}} + 2N_z L_1$. We vary only two of the three L_i parameters, since we aim to synchronize the metamaterial motion with that of the fluid, which in turn is characterized by two parameters, the wave number k_0^{fl} and the amplitude p_1^0.

Table II also lists the coarse-grained values in the optimized $(N_y \times N_z)$ metamaterials of ρ^{mm} as well as

TABLE II. Simulation results for the reference system and nine different optimized metamaterial systems illustrated in Fig. 3, all with $N_z = 2N_y$ and $d_0 = 0.1$ nm. Note that $L_3^{\mathrm{opt}} = L_3^0 = 67.9/N_y$ μm was kept fixed and not optimized; see Eq. (24).

Parameter	Ref. system	$(N_y \times N_z)$ metamaterial systems								
N_y	–	2	3	4	5	6	7	8	9	10
N_z	–	4	6	8	10	12	14	16	18	20
L_1^{opt} (μm)	–	199.8	138.6	106.7	86.3	72.1	62.0	54.4	48.4	43.6
L_2^{opt} (μm)	–	112.8	73.1	56.1	45.0	37.5	32.3	28.17	24.95	22.59
L_3^{opt} (μm)	–	34.0	22.63	16.98	13.58	11.33	9.70	8.49	7.54	6.79
$\rho^{\mathrm{mm}}/\rho_0^{\mathrm{fl}}$	–	0.988	0.985	0.975	0.972	0.973	0.970	0.970	0.970	0.969
$\mathrm{Re}[C_{yyyy}^{\mathrm{mm}}]\kappa_0^{\mathrm{fl}}$	–	1.306	1.083	1.030	0.996	0.990	0.985	0.970	0.958	0.968
$\mathrm{Re}[C_{zzyy}^{\mathrm{mm}}]\kappa_0^{\mathrm{fl}}$	–	1.673	1.374	1.484	1.479	1.475	1.500	1.472	1.444	1.484
$\mathrm{Re}[C_{yyzz}^{\mathrm{mm}}]\kappa_0^{\mathrm{fl}}$	–	1.673	1.374	1.484	1.479	1.475	1.500	1.472	1.444	1.484
$\mathrm{Re}[C_{zzzz}^{\mathrm{mm}}]/((2L_3/W_{\mathrm{cell}})\,\mathrm{Re}[C_{11}^{\mathrm{FS}}])$	–	0.939	0.960	0.949	0.948	0.948	0.946	0.948	0.950	0.947
H^{sl} (mm)	2.04	1.76	1.82	1.87	1.89	1.89	1.90	1.90	1.90	1.91
f_{res} (MHz)	1.920	2.051	1.980	1.977	1.972	1.967	1.970	1.965	1.959	1.965
$Q/10^4$	0.043	4.3	6.6	8.7	10.4	12.2	13.8	15.2	16.2	17.2
Q/Q^{ref}	1	99	153	200	240	283	321	351	375	397
$E_{\mathrm{ac}}^{\mathrm{fl}}$ (MJ/m^3)	8.1×10^{-6}	0.33	0.95	1.74	2.47	3.4	4.3	6.3	7.1	7.8
$\langle\langle v_2\rangle\rangle/v_2^{\mathrm{Rayl}}$	0.282	0.053	0.047	0.041	0.032	0.030	0.0264	0.0234	0.0213	0.0198

$\mathrm{Re}[C^{\mathrm{mm}}_{yyyy}]$ and $\mathrm{Re}[C^{\mathrm{mm}}_{zzyy}]$ relative to the predictions ρ_0^{fl} and $1/\kappa_0^{\mathrm{fl}}$, respectively, of the idealized analytical model. Also listed are $\mathrm{Re}[C^{\mathrm{mm}}_{yyzz}]$ and $\mathrm{Re}[C^{\mathrm{mm}}_{zzzz}]$, the latter compared to $(2L_3/W_{\mathrm{cell}})C^{\mathrm{FS}}_{11}$, which is the approximate value of two straight vertical struts, each of width L_3 distributed over the width W_{cell}. See the associated COMSOL script in the Supplemental Material [4] for the computation of these values.

B. Energy density and Q factor

In Fig. 3, the conventional reference cavity is compared with the optimized (5×10) metamaterial cavity. For the conventional cavity, the velocity amplitude of the acoustic mode in the bulk of the cavity, away from the boundary layers, is far greater than the wall velocity, leading to large velocity gradients inside the boundary layers near the fluid-solid interface. These gradients are much smaller inside the optimized metamaterial cavity because the first-order displacements $\mathbf{u}_1$ and $i\omega^{-1}\mathbf{v}_1$ are matched across the interface. This difference has a considerable effect on the Q factor of the mode, which in the following is always the $n = 1$ mode; henceforth we drop the mode index. The conventional cavity has $Q^{\mathrm{ref}} = 4.3 \times 10^2$, whereas the optimized (5×10) metamaterial cavity has $Q = 1.0 \times 10^5 = 240\, Q^{\mathrm{ref}}$, an enhancement of more than 2 orders of magnitude.

In Fig. 4(a) the acoustic energy density $E^{\mathrm{fl}}_{\mathrm{ac}}$ and the Q factor of the optimized systems are plotted against the number of unit cells N_y across the channel. For $N_y = 2$, the optimized systems already outperform the reference system for both metrics, and these performance metrics increase monotonically with N_y. For Q, this relationship is initially linear, whereas $E^{\mathrm{fl}}_{\mathrm{ac}}$ grows quadratically. At higher values of N_y, these increases taper off.

To illustrate the sensitivity of the optimized resonance modes to the geometric parameters, we show in Fig. 4(b) how the Q factor of the (5×10) metamaterial cavity mode decreases when L_1, L_2, and L_3 deviate from their respective optimized values. The greatest relative sensitivity is associated with L_1, where a 2% deviation from the optimum (1.5 μm away from 86.3 μm) halves the Q factor of the cavity. The greatest absolute sensitivity, however, is due to L_3, where a change of only 0.5 μm from the 13.58-μm optimum halves the Q factor of the cavity. Such sensitivity imposes severe restrictions on fabrication tolerances if one were to realize such a metamaterial device.

C. Streaming

To better understand the usefulness of the synchronized metamaterial cavities for acoustophoresis, we study the acoustic streaming field $\mathbf{v}_2$, as this provides a lower bound on the size of the particles that can be focused inside the cavity. For this reason, the streaming field of the optimized

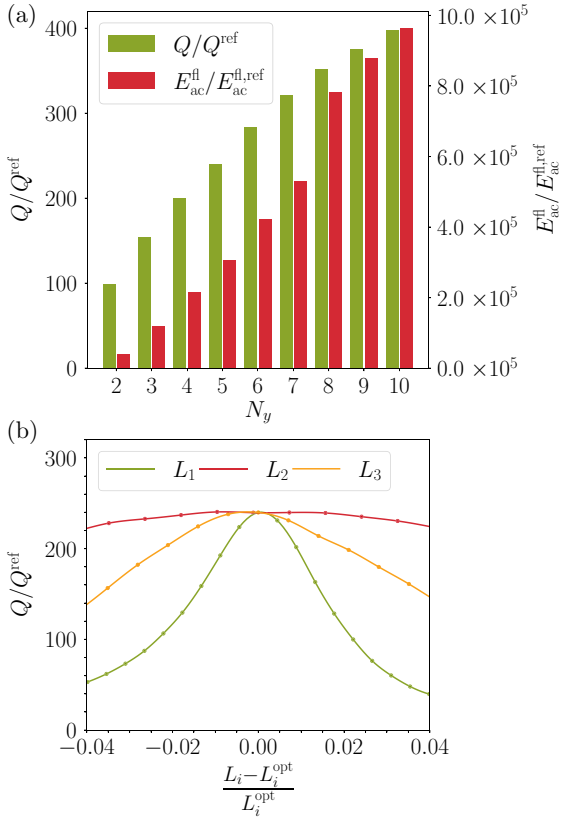

FIG. 4. (a) Simulated Q factors and acoustic energy density $E^{\mathrm{fl}}_{\mathrm{ac}}$ relative to the all-solid reference system (superscript "ref") for increasing numbers of unit cells N_y across the width of metamaterial regions with $d_0 = 0.1$ nm. (b) The normalized Q factor Q/Q^{ref} of the $N_y = 5$ cavity plotted against the relative deviation of either L_1, L_2, or L_3 from the optimum.

(5×10) metamaterial cavity is compared with that of the reference cavity. On the one hand, one would expect the synchronized cavity to produce less streaming than the reference cavity, since its boundary layers are considerably weaker. On the other hand, the many corners along the fluid-solid interface of the synchronized cavity tend to amplify the streaming [15]. That the former effect dominates is revealed in the last row of Table II, where it is seen that, in terms of the classical Rayleigh streaming velocity v_2^{Rayl} of Eq. (9b), the normalized streaming $\langle\langle v_2 \rangle\rangle / v_2^{\mathrm{Rayl}}$ is monotonically suppressed (nearly proportional to N_y^{-1}) by more than an order of magnitude when going from the reference cavity to the (10×20) metamaterial cavity. Such a tenfold reduction in the streaming speed implies a $\sqrt{10}$-fold decrease in the critical radius a_c from approximately 1 μm to approximately 300 nm, allowing significantly smaller particles to be focused.

We note in Fig. 5 that the streaming field of the synchronized metamaterial cavity is not only quantitatively but also qualitatively different from that in the reference cavity. Whereas the streaming field in the reference cavity

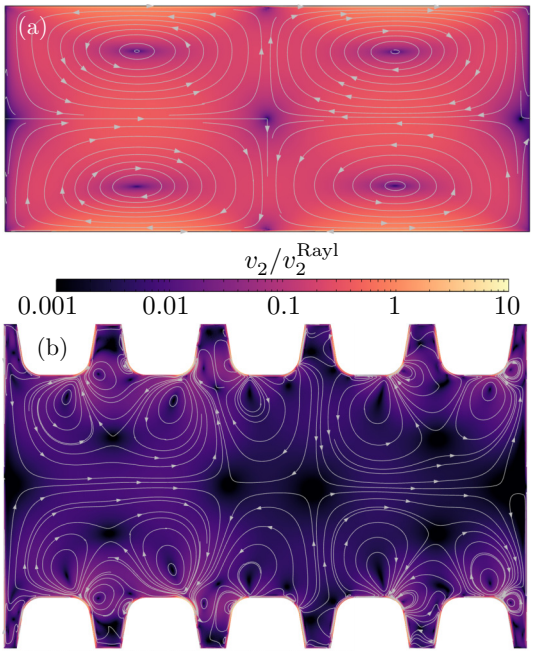

FIG. 5. Streaming fields $\mathbf{v}_2$ normalized by the Rayleigh streaming speed v_2^{Rayl} of Eq. (9b) inside (a) the reference cavity with $v_2^{\mathrm{Rayl}} = 8.3\ \mu\mathrm{m/s}$ and (b) the synchronized (5 × 10) metamaterial cavity $v_2^{\mathrm{Rayl}} = 2.5\ \mathrm{m/s}$. Both cases are actuated by $d_0 = 0.1$ nm. See the associated COMSOL scripts in the Supplemental Material [4].

is dominated by the conventional four large rolls filling the entire cross section, the streaming field in the synchronized cavity instead contains many smaller streaming vortices of various shapes and sizes. This results in a less uniform streaming pattern, but clearly with stronger suppression of the streaming $\langle\langle v_2\rangle\rangle \sim 0.02\, v_2^{\mathrm{Rayl}}$ in the middle third of the channel, $-\frac{1}{6}H^{\mathrm{fl}} < z < \frac{1}{6}H^{\mathrm{fl}}$, such that a_c decreases to approximately 150 nm in this region.

D. Particle focusing

A remarkable addition to the discussion of the critical particle size a_c is that the fluid pressure field p_1^{mm} in the synchronized metamaterial device scales with p_1^{ref} of the reference device and the Q factors, $p_1^{\mathrm{mm}} \sim (Q^{\mathrm{mm}}/Q^{\mathrm{ref}})\, p_1^{\mathrm{ref}}$. This relation implies that the acoustic radiation force F^{rad} on a suspended particle is a factor $(Q^{\mathrm{mm}}/Q^{\mathrm{ref}})^2 \sim 4 \times 10^4$ larger in the synchronized device than in the reference device for the same actuation amplitude, as is shown in Table II. Consequently, the focusing time $\tau \propto \eta(W^{\mathrm{fl}})^2/a^2E_{\mathrm{ac}}^{\mathrm{fl}}$ [16], or $\tau^{\mathrm{mm}} \propto (Q^{\mathrm{ref}}/Q^{\mathrm{mm}})^2\, (\eta(W^{\mathrm{fl}})^2/a^2E_{\mathrm{ac}}^{\mathrm{fl,ref}})$, is 4×10^4 times smaller in the former device than in the latter for a given particle size, corresponding to a reduction of more than 4 orders of magnitude in focusing time. Alternatively, a particle 2 orders of magnitude smaller, $a^{\mathrm{mm}} \sim 0.01a^{\mathrm{ref}}$, will focus in the same time in the metamaterial device as a^{ref} does in the reference device at the same actuation amplitude.

The dramatically improved nanoparticle acoustophoresis in the metamaterial device compared to the reference device is illustrated in Fig. 6. Here, the acoustophoretic velocity of 250-nm-radius nanoparticles increases by a factor of nearly 2×10^4, from 7 to 130 000 μm/s. Moreover, whereas no focusing is observed in the reference device even on the long time scale of 25 000 ms, the 250-nm-radius nanoparticles are focused in the metamaterial device near the vertical pressure node in the channel center in just about 3 ms. The acoustofluidic metamaterial device is not only able to focus smaller particles than the reference system, but the focusing is also very rapid.

V. EXTRUDING THE 2D MODEL TO A 3D MODEL

To check that the above results are not an artifact of working with a 2D model, we take the 2D cross section of Fig. 2 in the y-z plane and extrude it a length L along the x axis to create a 3D model defined for $-\frac{1}{2}L < x < \frac{1}{2}L$. We reduce the large number of mesh elements necessary to obtain convergent 3D simulations in two ways: (1) we study only the coarsest optimized metamaterial array listed in Table II, namely $(N_y, N_z) = (2, 4)$, and (2) we use our recently published boundary-layer model BL25 [5], in which the thin viscous boundary layer in the fluid (400 nm in water at 2 MHz) is taken into account analytically by adding additional terms in the boundary conditions at the fluid-solid interfaces, a procedure that circumvents the computer-memory-demanding resolution of the boundary layers.

The theory presented in Sec. II is the same as that used to derive the BL25 model, but besides simplifying the treatment of the viscous boundary layers, the acoustics in the fluid of the BL25 model reduces to a Helmholtz equation for the pressure p_1, and $\mathbf{v}_1$ is proportional to the gradient of p_1; see Eqs. (17a) and (17c) in Ref. [5]. This has the same form as the analytical model in Eq. (16).

The boundary conditions presented in Sec. II are the same in the 3D simulations, except for the BL25-model conditions on the first-order fields at the fluid-solid interface $\partial\Omega_{\mathrm{sl}}^{\mathrm{fl}}$. In addition, we must also specify the boundary conditions for all fields on the end boundaries $\partial\Omega_{\mathrm{end}}^{\mathrm{fl}}$, $\partial\Omega_{\mathrm{end}}^{\mathrm{sl}}$, and $\partial\Omega_{\mathrm{end}}^{\mathrm{mm}}$ for $x = \pm\frac{1}{2}L$. Here, we apply a simple clamping condition, where all motion is locked to zero along x, and transverse motion in the y-z plane is free. All these changes in boundary conditions for the 3D model are summarized in Table III.

In Fig. 7 the results of a simulation of the 3D model are shown using the same actuation amplitude $d_0 = 0.1$ as in the 2D model listed in Table I. When comparing these results obtained with the 3D extruded (2 × 4) metamaterial with those listed in Table II for the 2D (2 × 4) metamaterial, we find comparable results: $f_{\mathrm{res}}^{\mathrm{3D}} = 2.043\,74$ MHz

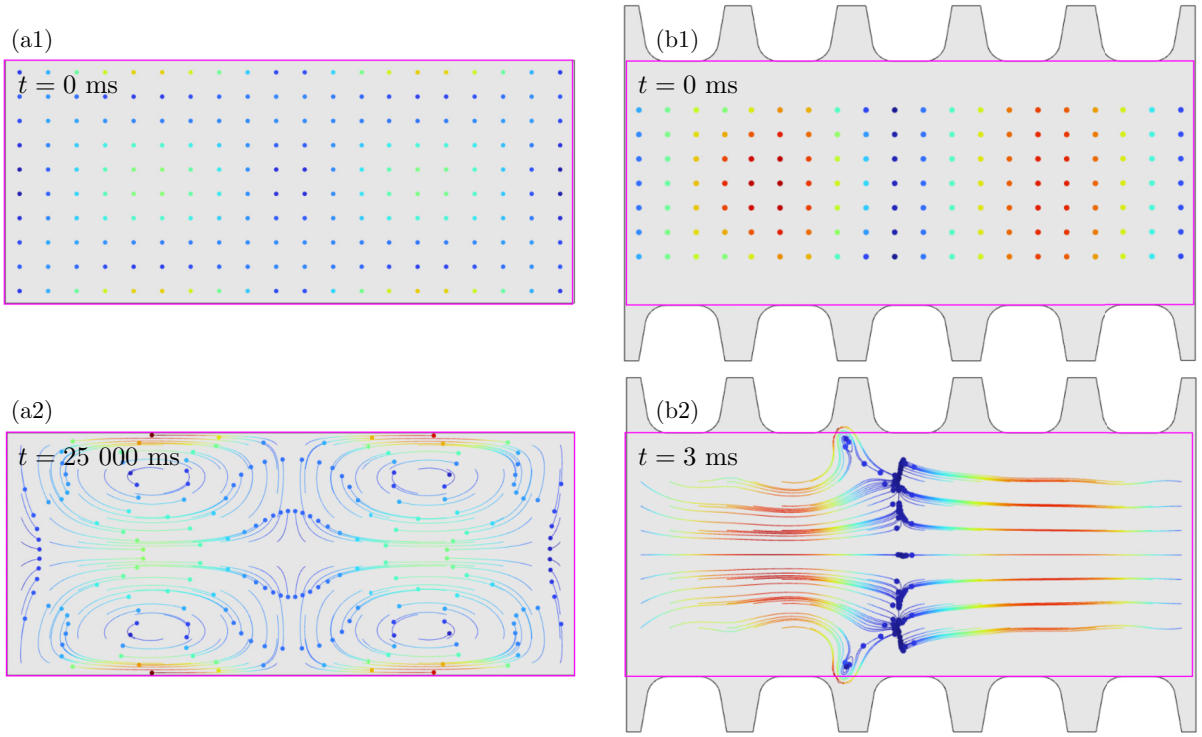

FIG. 6. COMSOL simulation of the acoustophoretic trajectories of 250-nm-radius polystyrene nanoparticles (dots) with initial positions on a regular grid. (a1) The reference device at $t = 0$ ms with initial velocities set equal to the local streaming velocity, represented by colors from 0 (dark blue) to 7 μm/s $\approx v_2^{\mathrm{Rayl}}$ (dark red). (a2) The same as panel (a1) but at $t = 25\,000$ ms, showing the individual trajectories (lines) colored according to speed along the trajectories using the same color scheme. (b1) Same as panel (a1) at $t = 0$ ms, but for the metamaterial devices and with velocity colors from 0 (dark blue) to 0.13 m/s $= 0.05\, v_2^{\mathrm{Rayl}}$ (dark red). (b2) The same as panel (b1) but at $t = 3$ ms, showing the individual trajectories (lines) colored according to speed along the trajectories using the same color scheme. Animated versions of the panels and associated COMSOL scripts are given in the Supplemental Material [4].

deviates by −0.2% from $f_{\mathrm{res}}^{\mathrm{2D}} = 2.051$ MHz, $Q^{\mathrm{3D}} = 4.7 \times 10^4$ deviates by 9% from $Q^{\mathrm{2D}} = 4.3 \times 10^4$, and $E_{\mathrm{ac}}^{\mathrm{res,3D}} = 0.37$ MJ/m^3 deviates by 12% from $E_{\mathrm{ac}}^{\mathrm{res,2D}} = 0.33$ MJ/m^3.

TABLE III. Boundary conditions specific to the 3D model.

Field	Boundary condition	Boundary
The fluid-solid interface; Eqs. (22), (23), (39) of Ref. [5]		
Effective slip for $\mathbf{v}_1$	$\mathbf{n}\cdot\nabla p_1 = \mathrm{i}\omega\rho_0^{\mathrm{fl}} v_1^{\mathrm{BL25}}$	$\Omega_{\mathrm{sl}}^{\mathrm{fl}}$
Stress continuity for $\mathbf{u}_1$	$\boldsymbol{\sigma}_1^{\mathrm{sl}}\cdot\mathbf{n} = \mathbf{f}_1^{\mathrm{BL25}}$	$\Omega_{\mathrm{sl}}^{\mathrm{fl}}$
Effective slip for $\mathbf{v}_2$	$\mathbf{v}_2 = \mathbf{v}_2^{\mathrm{BL25}}$	$\Omega_{\mathrm{sl}}^{\mathrm{fl}}$
Vertical end boundaries at $x = \pm\frac{1}{2}L$		
Clamped p_1 and $\mathbf{v}_1$	$\mathbf{e}_x\cdot\nabla p_1 = 0$	$\Omega_{\mathrm{end}}^{\mathrm{fl}}$
Clamped $u_{1,x}$	$u_{1,x} = 0$	$\Omega_{\mathrm{end}}^{\mathrm{sl}}$, $\Omega_{\mathrm{end}}^{\mathrm{mm}}$
Free u_{1y}, u_{1z}	$\sigma_{1,yx}^{\mathrm{sl}} = \sigma_{1,zx}^{\mathrm{sl}} = 0$	$\Omega_{\mathrm{end}}^{\mathrm{sl}}$, $\Omega_{\mathrm{end}}^{\mathrm{mm}}$
Clamped p_2	$\mathbf{e}_x\cdot\nabla p_2 = 0$	$\Omega_{\mathrm{end}}^{\mathrm{fl}}$
Clamped $v_{2,x}$	$v_{2,x} = 0$	$\Omega_{\mathrm{end}}^{\mathrm{fl}}$
Free v_{2y}, v_{2z}	$\sigma_{2,yx}^{\mathrm{sl}} = \sigma_{2,zx}^{\mathrm{fl}} = 0$	$\Omega_{\mathrm{end}}^{\mathrm{fl}}$

Finally, we note from Fig. 6(b2) that the focusing time for the 250-nm-radius polystyrene particles in the 2D (2 × 4) metamaterial can be estimated as $\tau_{(2\times4)}^{\mathrm{mm,2D}} \approx \tau_{(5\times10)}^{\mathrm{mm,2D}} Q_{(5\times10)}^2 / Q_{(2\times4)}^2 \approx (3\ \ \mathrm{ms}) \times (10.4/4.3)^2 \approx 18\ \ \mathrm{ms}$, and for the 3D model we see in Fig. 7(d) that $\tau_{(2\times4)}^{\mathrm{mm,3D}} \approx$ 8 ms. These numbers are of the same order of magnitude, and the difference between them is mainly due to the qualitative determination without a quantitative definition of the two focusing times $\tau_{(5\times10)}^{\mathrm{mm,2D}} \approx 3$ ms and $\tau_{(2\times4)}^{\mathrm{mm,3D}} \approx 8$ ms.

The streaming flow pattern in the 3D case is similar to that in the 2D case: the streaming flow in the axial x direction is negligible, and the streaming flow in the cross-sectional planes is suppressed as in the 2D case shown in Fig. 5, such that the resulting acoustophoretic motion leads to the observed nanoparticle focusing in the vertical x-z plane.

Even though the extruded (2 × 4) metamaterial was not optimized in the 3D model, we can conclude from this foray into 3D modeling that the velocity-matching, or synchronization, mechanism works equally well in the 3D

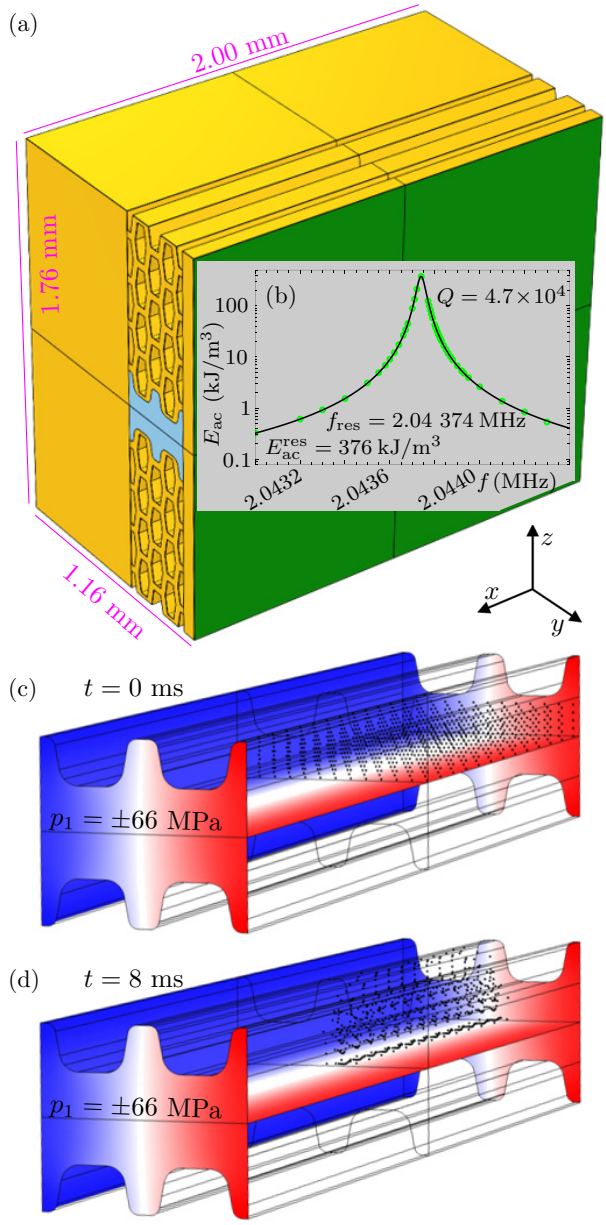

FIG. 7. (a) The geometry of the 3D model showing the solid (yellow), the two (2 × 4) metamaterials defined in Table II, the lid, the fluid channel (blue), and the actuation surface (green). (b) A semilog plot of the acoustic energy density $E_{\rm ac}$ for a water-filled channel embedded in the fused silica structure and actuated by a uniform actuation amplitude $d_0 = 0.1$ nm, as in Table I. The black line is a Lorentzian line fit to the green simulation points. The resonance frequency is $f_{\rm res}^{\rm 3D} = 2.043\,74$ MHz with $E_{\rm ac}^{\rm res} = 0.37$ MJ/m^3 and a Q factor of 4.7×10^4. (c) A uniform distribution of 250-nm-radius polystyrene nanoparticles (dots) at time $t = 0$ ms, analogous to the 2D (5 × 10) metamaterial shown in Fig. 6(b1). (d) The distribution of the focused particles at $t = 8$ ms, analogous to the 2D case in Fig. 6(b2). An animation of the panels is given in the Supplemental Material [4].

model as in the 2D model, and that it leads to enhanced Q factors in the 10^4–10^5 range, to the ability to focus nanoparticles, and to doing so on the millisecond time scale.

VI. DISCUSSION

The fraction of acoustic energy stored inside the fluid is $\bar{U}_{\rm ac}^{\rm fl}/\bar{U}_{\rm ac} \approx 0.2$ for the synchronized cavities. With the bulk damping factors $\gamma^{\rm fl} \approx 2 \times 10^{-5}$ and $\gamma^{\rm sl} \approx 6 \times 10^{-7}$, the theoretical upper bound for Q should therefore be [17]

$$Q^{\rm bulk} = \frac{\bar{U}_{\rm ac}}{\gamma^{\rm fl}\bar{U}_{\rm ac}^{\rm fl} + \gamma^{\rm sl}\bar{U}_{\rm ac}^{\rm sl}} \approx 2.2 \times 10^5. \tag{25}$$

In Table II we see that the cavities with a highly resolved (small-unit-cell) metamaterial tend to approach this theoretical upper bound quite well, and we may thus conclude that the fluid-solid matching, or synchronization, reliably removes the dissipation associated with the viscous boundary layers.

Looking ahead, if we speculate on how one may reduce this dissipation even further and thus obtain still higher Q factors, it should theoretically be possible to construct acoustic modes such that, at the whole-system resonance, the acoustic wave inside the fluid channel has a half-wavelength much longer than the fluid-channel width $W^{\rm fl}$, but still contains a pressure node. This would greatly reduce the bulk dissipation within the fluid.

We note that with the proposed cavities it is more difficult to diminish the streaming velocities than it is to increase the Q factors. As mentioned earlier, we attribute this to the many corners around the fluid channel [15], even though these corners have been somewhat rounded to avoid generating excessive streaming. One may therefore attempt to construct a cavity with fewer convex corners, or apply one of the methods proposed for suppression of acoustic streaming in previous work, such as shape optimization, inhomogeneous fluids, and counter-acting electro-osmosis [7,18,19]. Clearly, there are many ways to further suppress the remaining streaming.

With regard to how such synchronized cavities might be fabricated, one possibility is to rely on drawing towers such as those used for the fabrication of photonic-crystal optical fibers. We note that such drawing towers are already designed to shape fused silica glass with feature length scales smaller than those considered in this work [20]. Another possibility is to employ two-photon 3D printing and fabricate the metamaterial structure directly. This technique has recently been used to fabricate intricate micro- and nanoscale structures in glass with feature sizes much smaller than the minimum 5-μm scale encountered in our analysis [21].

We expect such delicate manufacturing techniques to have the added advantage of generating structures with very high strength. This is useful, as we have calculated the von Mises stress of our 2D metamaterial to peak at

3.5 GPa, a value slightly higher than the 2.7-GPa flexural strength of the fused silica flexures tested in Ref. [22].

The high acoustic energies achieved in this simulation are associated with correspondingly high acoustic pressure amplitudes (160 MPa in the 2D (5×10) metamaterial device), which are likely to cause cavitation within the fluid. At 1 MHz, a cavitation threshold of -26 MPa has been demonstrated in ultrapure degassed water [23]. Even if the cavitation threshold is higher at 2 MHz under fluid inertia, our proposed setup is likely to cause cavitation. This possibility serves as another demonstration of the effect of wall-fluid synchronization in acoustofluidic systems: cavitation may become a practical limitation for using the proposed metamaterial device for fast and efficient nanoparticle focusing. However, if cavitation is indeed observed in acoustofluidic metamaterial devices, such devices may be used as a tool to study the physics of ultrasound-induced cavitation.

The metamaterial system analyzed in this study constitutes an idealized proof-of-concept system. To develop this idea into a functional device requires substantial effort in designing a 3D system with actual transducers, electrical wiring, mechanical clamping, and inlet and outlet connectors to the microfluidic channel. All these aspects introduce additional dissipation, which threatens to lower the enhanced Q values of the metamaterial device. To meet some of these challenges, we suggest the following solutions. (1) Regarding the transducers, they could be chosen as thin-film transducers, as these offer very low dissipation [24,25]. (2) Regarding mechanical clamping and fluid connectors, a device much longer than the acoustic wavelength of the resonance mode could be envisioned, in which only the middle third is actuated by one or more attached thin-film transducers, and the two ends are clamped and provided with the necessary fluid connectors. Since the acoustic fields in acoustofluidics are known to decay on the length scale of the acoustic wavelength away from the actuation region [26], such a system would support an active region in the middle region with very large acoustic amplitudes and nearly zero amplitudes near the channel ends. As a result, the effect of mechanical clamping and attachment of fluid connectors at the ends would be negligible and would not lead to a significant contribution to the otherwise low dissipation of the system. (3) Exactly how to shape the metamaterial and where to place the thin-film transducers in the active region goes beyond our simple design of Fig. 7. This problem may be addressed using topology optimization, which has previously been applied to optimize microelectromechanical resonators [27].

VII. CONCLUSION

By using metamaterials in acoustofluidic systems, we have demonstrated that, under ideal circumstances, it is possible to dramatically reduce the acoustic boundary layers by synchronizing the motion of the fluid with that of the adjacent solid walls. This in turn removes the viscous friction near the fluid-solid interface and may also, to a lesser extent, reduce the acoustic streaming. This technique of using acoustic metamaterials to remove viscous friction could help increase Q factors in a wider range of microelectromechanical systems. Specifically for acoustophoretic focusing of particles, synchronized metamaterial cavities may lead to a reduction of the critical particle size for focusing of nanoparticles and to faster focusing of nanoparticles compared with the current state of the art using cavities in conventional materials. We hope that this theoretical and numerical proof-of-concept work, with its albeit idealized 2D and 3D modeling, will inspire experimental efforts to fabricate such high-Q-factor acoustofluidic devices.

ACKNOWLEDGMENTS

This work was supported by the *PRISMA* project funded by the European Innovation Council (EIC), HORIZON EIC 2022 TRANSITION, Grant No. 101057436.

DATA AVAILABILITY

The data that support the findings of this article are openly available [4].

[1] R. Barnkob, P. Augustsson, T. Laurell, and H. Bruus, Measuring the local pressure amplitude in microchannel acoustophoresis, Lab Chip **10**, 563 (2010).

[2] J. S. Bach and H. Bruus, Theory of pressure acoustics with viscous boundary layers and streaming in curved elastic cavities, J. Acoust. Soc. Am. **144**, 766 (2018).

[3] A. da S. Marques and G. Tomaz da Silva, Vortex modes in acoustofluidic cylindrical resonators, J. Fluid Mech. **1015**, A34 (2025).

[4] See Supplemental Material at http://link.aps.org/supplemental/10.1103/vcxl-g1pb for animated gifs of Figs. 3, 6, and 7, and for COMSOL scripts associated with Figs. 3, 5, and 6.

[5] S. Z. Hoque and H. Bruus, Boundary-layer modeling of polymer-based acoustofluidic devices, Phys. Rev. Appl. **24**, 044095 (2025).

[6] L. P. Gorkov, On the forces acting on a small particle in an acoustical field in an ideal fluid, Sov. Phys. Dokl. **6**, 773 (1962). [Dokl. Akad. Nauk SSSR **140**, 88 (1961)].

[7] J. S. Bach and H. Bruus, Suppression of acoustic streaming in shape-optimized channels, Phys. Rev. Lett. **124**, 214501 (2020).

[8] B. G. Winckelmann and H. Bruus, Acoustic radiation force on a spherical thermoviscous particle in a thermoviscous fluid including scattering and microstreaming, Phys. Rev. E **107**, 065103 (2023).

[9] P. B. Muller, R. Barnkob, M. J. H. Jensen, and H. Bruus, A numerical study of microparticle acoustophoresis driven by acoustic radiation forces and streaming-induced drag forces, Lab Chip **12**, 4617 (2012).

[10] R. Barnkob, P. Augustsson, T. Laurell, and H. Bruus, Acoustic radiation- and streaming-induced microparticle velocities determined by microparticle image velocimetry in an ultrasound symmetry plane, Phys. Rev. E **86**, 056307 (2012).

[11] Onda, *Tables of Acoustic Properties of Materials: Solids* (Onda Corporation, Sunnyvale (CA), USA, 2003), https://www.ondacorp.com/wp-content/uploads/2020/09/Solids.pdf, accessed 30 April 2026.

[12] P. B. Muller and H. Bruus, Numerical study of thermoviscous effects in ultrasound-induced acoustic streaming in microchannels, Phys. Rev. E **90**, 043016 (2014).

[13] B. Ling, K. Wei, Z. Wang, X. Yang, Z. Qu, and D. Fang, Experimentally program large magnitude of Poisson's ratio in additively manufactured mechanical metamaterials, Int. J. Mech. Sci. **173**, 105466 (2020).

[14] COMSOL, *COMSOL Multiphysics 6.3*, (COMSOL AB, Stockholm, Sweden, 2024), http://www.comsol.com.

[15] M. Ovchinnikov, J. Zhou, and S. Yalamanchili, Acoustic streaming of a sharp edge, J. Acoust. Soc. Am. **136**, 22 (2014).

[16] R. Barnkob, I. Iranmanesh, M. Wiklund, and H. Bruus, Measuring acoustic energy density in microchannel acoustophoresis using a simple and rapid light-intensity method, Lab Chip **12**, 2337 (2012).

[17] P. Hahn and J. Dual, A numerically efficient damping model for acoustic resonances in microfluidic cavities, Phys. Fluids **27**, 062005 (2015).

[18] J. T. Karlsen, W. Qiu, P. Augustsson, and H. Bruus, Acoustic streaming and its suppression in inhomogeneous fluids, Phys. Rev. Lett. **120**, 054501 (2018).

[19] B. G. Winckelmann and H. Bruus, Theory and simulation of electroosmotic suppression of acoustic streaming, J. Acoust. Soc. Am. **149**, 3917 (2021).

[20] K. Tajima, J. Zhou, K. Nakajima, and K. Sato, Ultralow loss and long length photonic crystal fiber, J. Lightwave Technol. **22**, 7 (2004).

[21] J. Bauer, C. Crook, and T. Baldacchini, A sinterless, low-temperature route to 3D print nanoscale optical-grade glass, Science **380**, 960 (2023).

[22] Y. Bellouard, On the bending strength of fused silica flexures fabricated by ultrafast lasers [invited], Opt. Mater. Express **1**, 816 (2011).

[23] E. Herbert, S. Balibar, and F. Caupin, Cavitation pressure in water, Phys. Rev. E **74**, 041603 (2006).

[24] A. G. Steckel, H. Bruus, P. Muralt, and R. Matloub, Fabrication, characterization, and simulation of glass devices with AlN thin-film transducers for excitation of ultrasound resonances, Phys. Rev. Appl. **16**, 014014 (2021).

[25] A. G. Steckel and H. Bruus, Numerical study of bulk acoustofluidic devices driven by thin-film transducers and whole-system resonance modes, J. Acoust. Soc. Am. **150**, 634 (2021).

[26] O. Manneberg, S. M. Hagsäter, J. Svennebring, H. M. Hertz, J. P. Kutter, H. Bruus, and M. Wiklund, Spatial confinement of ultrasonic force fields in microfluidic channels, Ultrasonics **49**, 112 (2009).

[27] D. Giannini, N. Aage, and F. Braghin, Topology optimization of MEMS resonators with target eigenfrequencies and modes, Eur. J. Mech. A: Solids **91**, 104352 (2022).